Wall-modeled large eddy simulation in complex geometries with application to high-lift devices

By J. Bodart AND J. Larsson

1. Motivation and objectives

In large eddy simulations (LES) of wall-bounded flows, the need to resolve energy-carrying eddies in the vicinity of the wall leads to a prohibitive cost which prevents its use at very high Reynolds numbers. To overcome this limitation, many attempts have been made in the last two decades to model the unresolved scales near the wall. These works mainly focused on two different approaches: hybrid RANS/LES computations and direct modeling of the wall-stress. In hybrid RANS/LES, the unsteady Navier-Stokes equations are solved on a single grid with the eddy viscosity computed from a RANS model near the wall and a LES model away from the wall. In the wall-stress modeling approach, the LES equations are formally defined everywhere in the domain, with RANS equations solved on an embedded (overlapping) grid near the wall. The coupling between RANS and LES is weaker and acts in a fashion similar to the widely used wall-functions in RANS: the RANS solver takes information from the computed LES flow field, and returns back the result in the form of wall fluxes, i.e., the shear stress and heat transfer at the wall. The present contribution falls into the second category and is aimed at evaluating the benefits of this approach in situations involving complex geometries and underlying complexity in the flow field, such as transition and/or separation. Wall-modeling in the context of LES dates back four decades, but has primarily been applied to problems with simple geometry, e.g., the turbulent flow in a channel. Balaras *et al.* (1996) extended the modeling to account for some non-equilibrium effects and applied this to duct flow. Wang & Moin (2002) added a dynamic procedure to the non-equilibrium model and applied it to the flow over a trailing edge. More recently, a non-equilibrium model has been developed and tested in a channel flow with periodic hills (Duprat *et al.* 2011). To the authors' knowledge, no attempts have been made so far to use a wall-model approach in a configuration where the geometric complexity requires the use of an unstructured grid. Here we aim at evaluating the concept for external aerodynamics at high Reynolds number and identify the remaining challenges.

This brief is organized as follows: we first describe the strategy for implementation of the wall model in a general unstructured grid and discuss the overall computational performance. We then present preliminary results obtained for the flow around the McDonnell-Douglas 30P/30N airfoil, a three-element high-lift system, to evaluate the accuracy of the global procedure. This case is run with a Reynolds number of $Re_c = 9.6 \cdot 10^6$, based on the stowed chord length, which is at the limit of what is affordable on the biggest available computers with traditional wall-resolved LES. We find excellent agreement with experiments for the pressure coefficient C_p, as well as for the lift coefficient C_l, although the results for the velocity field are not sufficiently accurate. We argue and show that dynamically switching the wall-model on/off in response to a local flow sensor is an im-

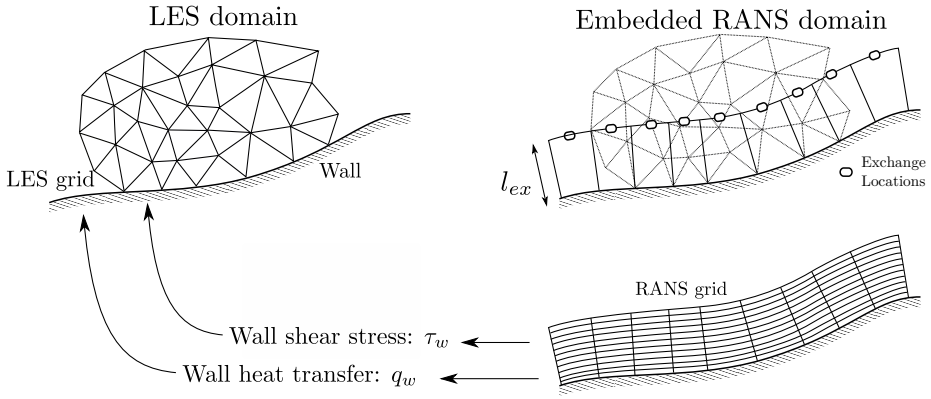

FIGURE 1. Sketch of the wall-modeling procedure.

portant step towards accurate and predictive wall-modeled LES, and demonstrate that a simple sensor significantly improves the accuracy of the predicted velocity field.

2. Wall-model integration in an unstructured solver

The wall-model is added to the in-house massively-parallel solver CharLES, in which the spatially-filtered compressible Navier-Stokes equations are solved. This code uses a finite volume approach, with second order schemes in space and low numerical dissipation and a third-order Runge-Kutta scheme for explicit time advancement. The Smagorinsky subgrid scale model is used to account for the unresolved motions, together with a dynamic evaluation of the Smagorinsky coefficient (Germano *et al.* 1991). The cell-centered formulation allows for a straightforward implementation of Neumann-type (i.e., flux) boundary conditions.

2.1. *Wall-model*

An external module is first developed to handle the wall-model. At this stage we consider a wall surface and an associated surface where the flow field variables (e.g., u,T) are known from the LES computation. The compressible equilibrium boundary layer equations are solved between these surfaces in a fashion similar to the work of Kawai & Larsson (2012). The equations reduce to the coupled system of ODEs

$$\frac{\mathrm{d}}{\mathrm{d}\eta}\left((\mu+\mu_{t,wm})\frac{\mathrm{d}u_\parallel}{\mathrm{d}\eta}\right) = -S_m(\eta)\,, \tag{2.1}$$

$$\frac{\mathrm{d}}{\mathrm{d}\eta}\left((\mu+\mu_{t,wm})u_\parallel\frac{\mathrm{d}u_\parallel}{\mathrm{d}\eta} + (\lambda+\lambda_{t,wm})\frac{\mathrm{d}T}{\mathrm{d}\eta}\right) = -S_e(\eta)\,, \tag{2.2}$$

where η refers to the wall-normal coordinate, $u_\parallel$ the wall-parallel velocity component, μ the dynamic viscosity, and λ the thermal conductivity. For this equilibrium model, the three-dimensional PDE system becomes a set of independent 1D ODEs (for each wall face), which associates one wall face and a corresponding EL, and can be solved in a sequential manner. The eddy viscosity $\mu_{t,wm}$ is obtained from the mixing-length model

$$\mu_{t,wm} = \kappa\eta\sqrt{\rho\tau_w}\left[1-\exp\left(-\frac{\eta^+}{A^+}\right)\right]^2 \quad \text{with } A^+=17,\ \kappa=0.41\,. \tag{2.3}$$

The turbulent thermal conductivity $\lambda_{t,wm} = \mu_{t,wm} c_p / Pr_{t,wm}$ is obtained using a constant turbulent Prandtl number $Pr_{t,wm} = 0.9$. The momentum/energy source terms S_m and S_e may in general include contributions from the pressure gradient or the convective terms but are set to zero in this work, in order to evaluate the full potential of equilibrium models. Curvature effects are neglected ($\delta/R_c \ll 1$), which is a reasonable assumption given the high Reynolds number of our applications. The two coupled equations are solved one at a time, using a second-order finite-volume approach. The resulting tridiagonal matrix is inverted with a direct solver (Thomas algorithm). The procedure is repeated until convergence is reached, which typically requires less than ten iterations.

2.2. *A grid-independent exchange location*

Whereas the wall-modeling implementation is generally trivial in a structured solver, it requires a bit more effort when going to unstructured grids/solvers. For its usefulness in industrial configurations, the methodology should be : (a) suitable to any kind of unstructured grid and (b) compatible with massively parallel solvers. The location from which the information extracted to feed into the wall-model, hereafter referred to as the Exchange Location (EL), is of particular interest. Kawai & Larsson (2012) recently showed that moving the EL away from the wall significantly reduces the numerical errors and improves the accuracy of the resulting LES computation. Thus, the EL should be independent of the mesh nodes. We recall that common practice in the context of structured meshes uses the first cell center off the wall as the EL. In our case, the EL becomes a parameter of the simulation, which can be adjusted according to the flow field characteristics. To set the EL requires knowledge of the boundary layer thickness, which is a property of the solution. Although unsatisfactory, this is no different from the general status of grid-generation (that the basic features and length scales of the solution decide what mesh-spacing is needed). From a computational point of view, the main downside in using an EL remote from the first adjacent wall cells lies in the domain decomposition. Indeed, a wall face and its corresponding EL in the LES grid may not exist on the same processor after the domain decomposition. This is solved here by connecting each wall face with its EL during a pre-processing step, using parallel communicators that are then used during the computation.

2.3. *Building the wall-model mesh*

To solve the wall-model requires a grid between the wall and the EL. This grid is generated during a pre-processing step using a simple extrusion of the wall surface mesh along the normal vector of each wall face and results in a structured and locally orthogonal mesh for the wall-model. Unlike the outer grid, which may be fully unstructured, it is convenient to use an embedded structured grid in the vicinity of the wall, mainly for two reasons:

- for the 1D equilibrium ODE formulation used here, the equations are most naturally solved along lines normal to the wall;
- if solving the full 3D RANS equations, a structured grid provides a straightforward way to solve the wall-normal direction implicitly in time.

The last point is particularly critical for compressible solvers with explicit time integration owing to the acoustic CFL limitation. The wall-model grid must satisfy $n^+ \approx 1$, which with an explicit time-integration would lead to extremely small time steps. In fact, the wall-model solver can be regarded in this case as a zonal solver, which removes the wall-induced CFL limitation for a compressible LES solver. Although this is not its primary function, it is undoubtedly a second advantage of this approach.

Finally, we stress that this method is suitable for most geometries: given the small thickness of boundary layers at high Reynolds number, it is highly unlikely that the curvature of the geometry prevents the use of this extrusion, at least in external aerodynamic problems. We choose to extrude the wall surface mesh at the pre-processing stage using a user-defined distance parameter l_{ex} as described in Fig. 1. It is thus possible to take into account the recommendations suggested by the work of Kawai & Larsson (2012), which states that a minimum of three LES cells should lie between the wall face and the associated EL.

2.4. *Resulting LES boundary conditions and implementation efficiency*

The final LES boundary conditions are sketched in Fig. 1. As the EL does not necesarily match with the face/nodes in the LES grid, an interpolation procedure is required at runtime. This is done using the simple formula

$$u_i^{EL} = u_i^{fa} + \frac{\partial u_i}{\partial x_j}(x_j^{EL} - x_j^{fa}), \tag{2.4}$$

where the superscript fa refers to the face center closest to the EL in the domain. The viscous flux at the wall is assumed to be aligned with the velocity vector at the EL, thereby making the assumption that the direction of the shear does not change in the unresolved part of the boundary layer, i.e.,

$$(\tau_{ij} n_j)_{w,LES} = \tau_{w,wm}\ e_{\parallel i}\ , \tag{2.5}$$

with $e_\parallel$ a unit vector parallel to the wall and aligned with the velocity.

The extra cost incurred by the procedure is likely to be negligible in an incompressible solver in which a Poisson equation has to be solved. In compressible solvers, which are usually fully explicit in time, the cost of the wall-model can be prohibitive. We observed that in the cases run so far for different applications, the number of points needed in the LES grid is roughly to the number of grid points use by the wall-model, which could lead to the same one-to-one ratio for the computational cost (when solving the full 3D RANS equations). To limit the cost, we choose to update the boundary flux only once per time step, instead of at each Runge Kutta substep. This was found to have a negligible effect on the accuracy. The extra cost of the wall-model is about 30% of the stand-alone LES cost. However, no optimization has been performed on the load-balance at this stage, meaning that a processor having n wall cells will solve the same number of associated wall-model equations. A perfect load-balancing of the wall-model procedure would reduce the cost to 5% in the cases we have considered.

3. Turbulent channel flow

We perform a set of turbulent channel flow simulations as a first validation of the method. The main purpose of these tests is to retrieve the results established with structured solvers, but also to evaluate the degree of accuracy of the interpolation method used. The DNS data of the turbulent channel flow at $Re_\tau = 2000$ (Hoyas & Jiménez 2006) is used as a reference solution. A constant mass-flow rate is enforced throughout the simulation using a dynamically adjusted forcing term in the momentum equation. The power induced by this forcing term is balanced in the energy equation by heat transfer at the wall, where the wall-model with constant wall temperature is applied. The Mach number is kept around the incompressibility limit close to $M = 0.3$ based on the centerline flow conditions. Statistical convergence is reached when the energy equation is fully balanced.

	L_x/δ	L_y/δ	L_z/δ	$n_x\delta/L_x$	$n_y\delta/L_y$	$n_z\delta/L_z$
CHA	25	2	10	5	8	25
CHB	25	2	10	10	16	50

TABLE 1. Turbulent channel flow simulations: mesh size and resolution, where δ is the channel half-height.

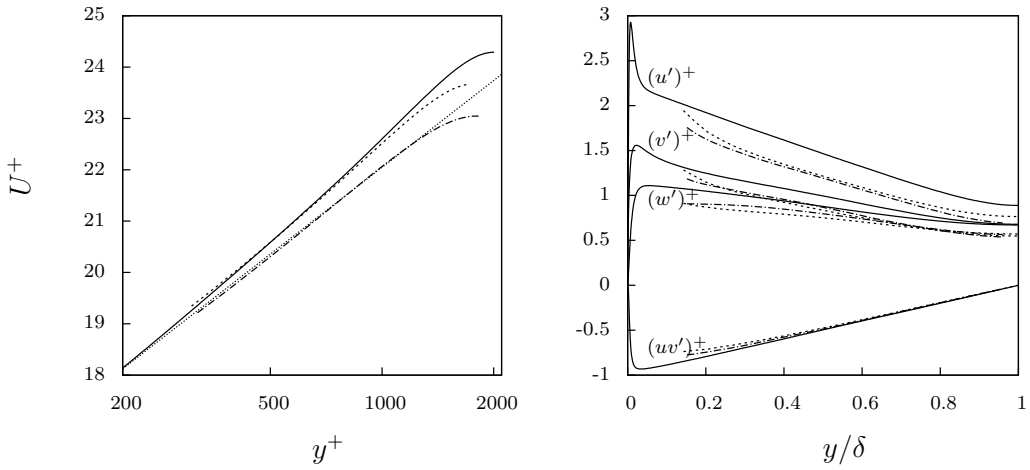

FIGURE 2. Channel flow simulations: *left* - Velocity profile, with Van Driest transformation. *right* - Resolved part of the Reynolds-stress tensor. (—) DNS by Hoyas & Jiménez (2006), (- - -) CHA, (----) CHB, (·····) log law with $C = 0.52$.

As this convergence process can take several tens of flow-through times, the simulation is first advanced on a very coarse grid. The final results are obtained by gathering statistics over more than ten flow-through times tU_b/L_x, during which the total energy variation is found to be less than 0.01%. Two grids are used, with details listed in Table 1. The matching location was set to $l_{ex} = 0.15\delta$, where δ is the channel half-height.

The velocity profiles are shown in Fig. 2. The Van Driest transformed profile obtained with the finest grid CHB compares very well with the (incompressible) DNS data of Hoyas & Jiménez (2006). The importance of the outer-layer grid resolution is demonstrated by the results obtained with the coarser grid (CHA): the velocity profile is significantly different, which proves the inaccuracy induced by such a coarse resolution, independently of the wall-model itself. The resolved part of the Reynolds-stress tensor (also shown in the figure) agrees well with existing LES results. This shows that high-Reynolds-number simulations with a wall-model can be performed with an excellent degree of accuracy if sufficient mesh resolution is maintained in the outer LES grid.

3.1. *EL interpolation procedure*

To evaluate the accuracy of this interpolation procedure, we apply the wall-model using the same EL but with two different interpolation procedures. The EL is set exactly at a cell center location in the LES grid. Either the upper face (case I-Up) or the lower face (case I-Lo) is used to perform the interpolation, as described in Fig. 3. The two cases are run on grid CHB and are started using the same initial conditions. The time evolution

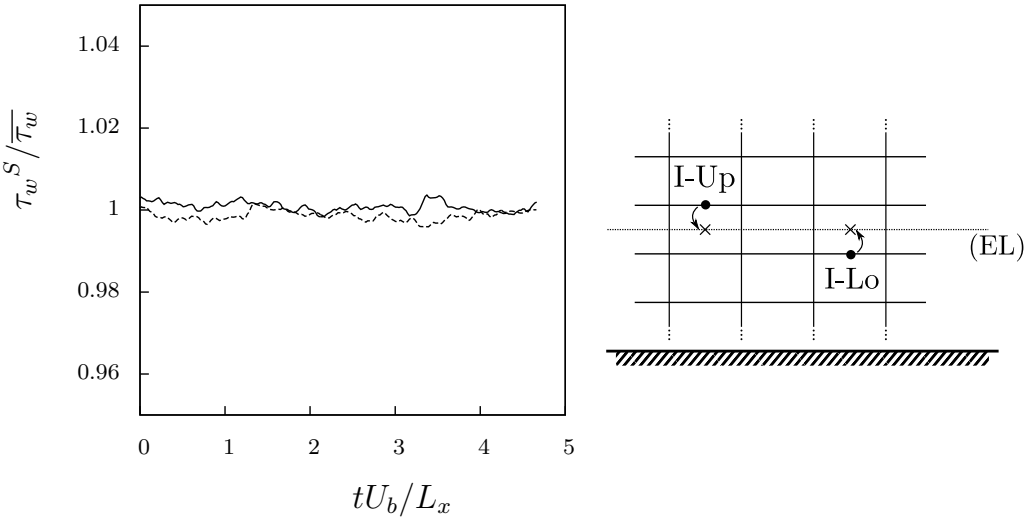

FIGURE 3. Validation of the interpolation procedure: spatially averaged wall shear stress. (—) I-Up, (----) I-Lo.

of the wall shear stress (spatially averaged over the two walls) is presented in Fig. 3. Although there is a slight difference in the shear stress between the two cases, this stays below 0.5%; this shows that this simple interpolation procedure is sufficiently accurate for our needs.

4. McDonnell-Douglas 30P/30N multi-element airfoil

To evaluate the accuracy of wall-modeled LES applied to a realistic and complex flow, we compute the flow around a McDonnell-Douglas 30P/30N multi-element airfoil at high angle of attack. This test case involves several flow complexities that challenge the wall-model, in particular flow separation and transition to turbulence. The complexity of flows around general high-lift systems is described in detail by Rumsey (2002). Much experimental data is available for this case, especially from NASA Langley (Chin *et al.* 1993; Klausmeyer & Lin 1994) where a large experimental program has been devoted to high-lift systems. The main limitation of RANS models is their inability to predict transition location and their inaccuracy in separated flows. Traditional LES does not suffer from these limitations but becomes exceedingly expensive when applied at realistic Reynolds numbers. The proposed wall-modeled LES approach reduces by two orders of magnitude the required number of grid points in comparison with typical wall-resolved LES for this test case (D. You, unpublished work) at the realistic Reynolds number of $Re_c = 9.6 \cdot 10^6$ (based on the chord length c and the free-stream velocity U_∞). We focus here on a configuration close to stall, with an angle of attack $\alpha = 19^\circ$ and a free-stream Mach number $M = 0.2$.

4.1. *Numerical set-up and flow topology*

Preliminary results have been obtained on a relatively coarse grid. Although the implementation can use any kind of unstructured grid, we first use a hybrid grid, structured near the wall and unstructured in the far-field. This reduces the numerical errors induced by non-hexaedral cells. A slice of the mesh and the computational domain are shown in

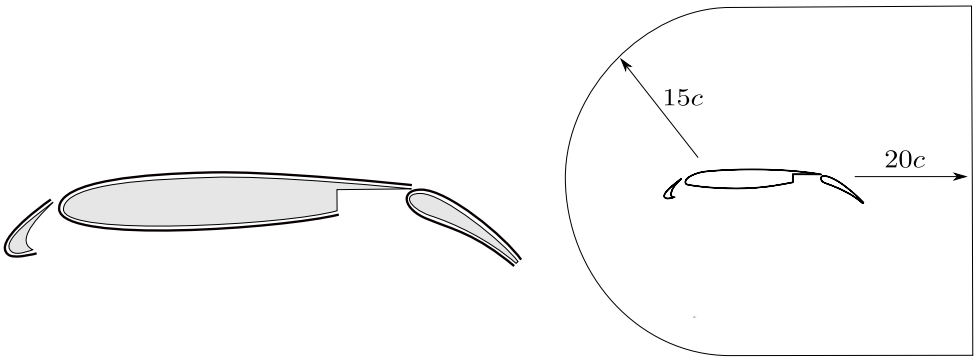

FIGURE 4. *left* - The MD 30P/30N multi-element airfoil with thick plain lines where the wall model is applied. *right* - Associated computational domain extent.

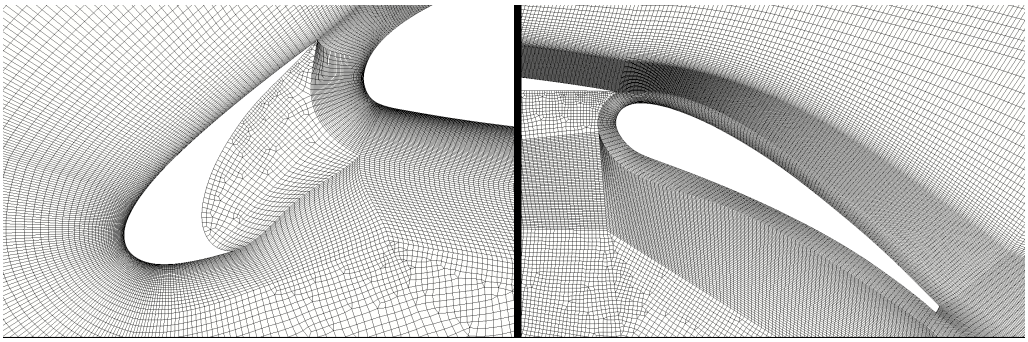

FIGURE 5. Grid overview: *left* - Slat region. *right* - Flap region.

Figs. 4 and 5. The spanwise direction is discretized using 50 cells over a distance of $L_z = 0.04c$ and is assumed to be periodic. Non-reflective boundary conditions are applied at the inflow/outflow. A total of 7.3 million cells are used, and roughly 50,000 CPU hours on the local Certainty cluster are required for a single, converged run.

To ensure fully converged statistics, the solution is advanced during $T = 20U_\infty/c$. Although most of the flow characteristics are established after $T = U_\infty/c$, slow convergence to a statistically steady state is experienced at the leading edge of the slat, as illustrated by the convergence history of the lift and drag coefficients for the slat in Fig. 6.

The streamlines of the mean flow-field are shown in Fig. 7. Given the large angle of attack, the stagnation points are located far from the leading edge on the pressure side of both the slat and the main element. If we disregard the coves on the slat and the main element where strong recirculations occur, the flow is fully attached except near the slat transition location where a laminar separation bubble occurs due to the strong adverse pressure gradient in this region. At this stage, it is too early to state that the recirculation is not a wall-model artifact, as this sensitive feature of the flow is captured with only two cells in the wall-normal direction. However, in his work on transition measurements on the same airfoil, Bertelrud (1998) mentioned that, for $\alpha > 8°$ "transition is nearly instantaneous" and could occur "through a closed separation bubble". Contrary to RANS simulations, no tripping is required for transition and turbulence develops by itself. The predicted transition point is not fully physical as it is triggered by numerical noise. However, the small disturbances amplify sufficiently quickly so that the predicted transition point does not depend too critically on the initial disturbance. In future work,

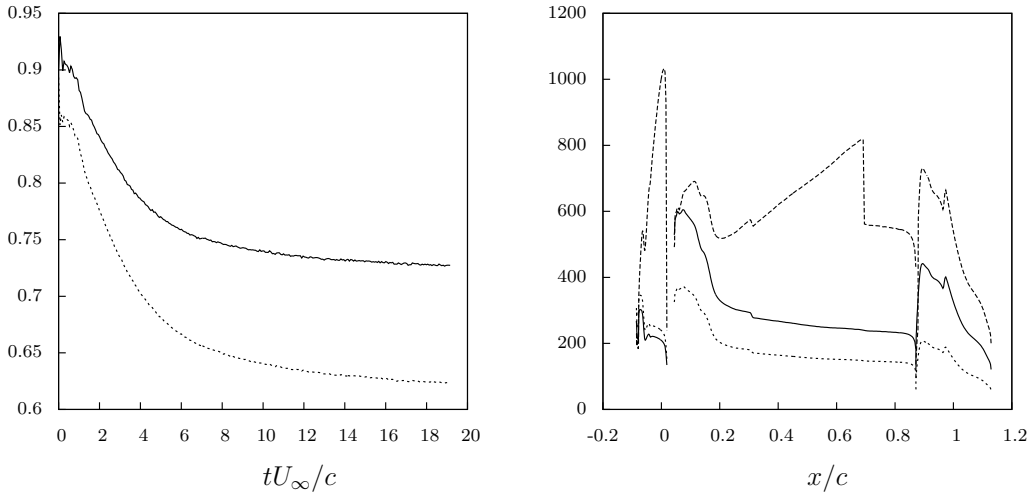

FIGURE 6. *left* - Convergence history of the slat lift and drag coefficients for the WM case. (—) C_l, (----) -C_d. *right* - Wall-adjacent cell size in wall units, based on the computed wall shear stress. x_1 and x_2 refers to respectively the wall-tangent and the spanwise direction. (—) l^+_{ex}, (----) Δx^+_1, (····), Δx^+_2.

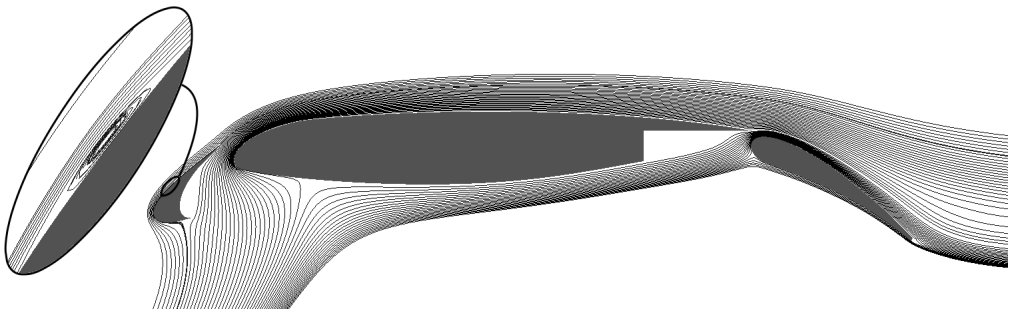

FIGURE 7. Streamlines around the MD 30P/30N configuration at 19° angle of attack.

free-stream turbulence will be added, and the grid-independency of this result will be verified in order to perform meaningful comparisons with experiments. We first discuss two simulations computed with (a) the usual no-slip boundary condition applied everywhere (NOWM case) and (b) a wall-model applied in all the regions where attached boundary layers develop as described in Fig. 4 (WM case).

4.2. *Results: aerodynamic coefficients*

Very good agreement is found for the surface pressure coefficient, as presented in Fig. 8. Although the pressure field is mainly imposed by the geometry of the airfoil, significant improvements are found in comparison with the NOWM case, in which the wall shear stress is seriously under-estimated. The resulting drag and lift coefficients are also well predicted and very close to experimental values (see Table 2). The wall-modeled LES gives very good result in the flap region where the boundary layer is thick and turbulent except very near the leading edge. The simple equilibrium wall-model seems sufficient to compute the aerodynamic coefficients with relatively good accuracy. However, a final judgment must await a grid-convergence study.

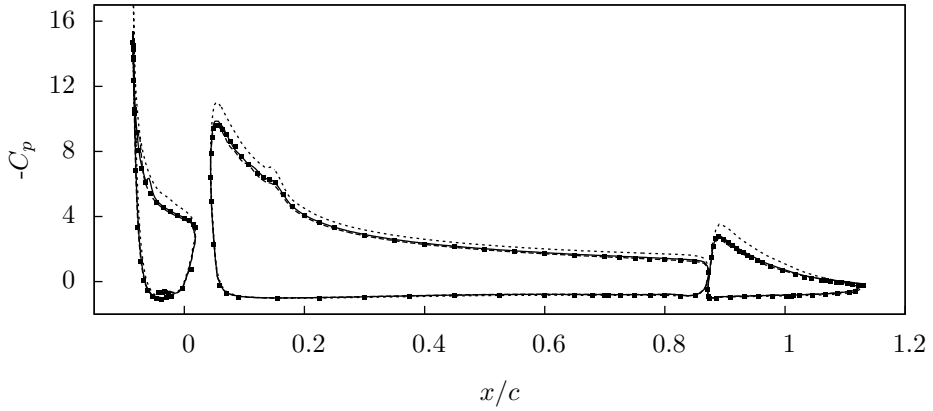

FIGURE 8. Surface pressure coefficient. (■) Experiments by Chin *et al.* (1993), (—) DLTS, (- -) WM, (····) NOWM.

	C_l				C_d			
	Slat	Main	Flap	Total	Slat	Main	Flap	Total
DLTS	0.75	3.19	0.36	4.30	-0.651	0.420	0.333	0.102
WM	0.73	3.11	0.36	4.20	-0.622	0.409	0.318	0.105
NOWM	0.85	3.51	0.43	4.79	-0.792	0.461	0.396	0.065
Experiments	**0.75**	**3.14**	**0.37**	**4.27**	-	-	-	-

TABLE 2. Integrated aerodynamic coefficients, comparison with experiments.

4.3. *Results: laminar/turbulent switching*

The obvious over-estimation of the wall shear stress accompanying the use of the wall-model in laminar regions suggests switching off the wall-model in these regions. To validate this idea, a simple flow sensor is designed to identify laminar and turbulent regions. Given the two-dimensional geometry studied, it is clear that non-zero spanwise velocity fluctuations are associated with turbulent motions. At each time step, we compare the local value of the spanwise velocity at the EL with a fixed threshold value. For low (essentially zero) spanwise velocity, classic no-slip boundary conditions are applied, whereas the wall-model is applied elsewhere. This sensor is surely not universal and presents some obvious downsides:

- The optimum threshold value is necessarily different on the three different airfoil elements because the outer velocity is different for each.
- The threshold value is dependent on the EL distance, which again makes it very sensitive to the airfoil element considered.
- In an instantaneous flow field, a turbulent region can locally have a spanwise velocity small enough to turn off the wall-model.
- As the sensor takes information at the EL, this leads to erroneous results at the laminar separation bubble, because the EL is located above the recirculation bubble where the flow is turbulent.

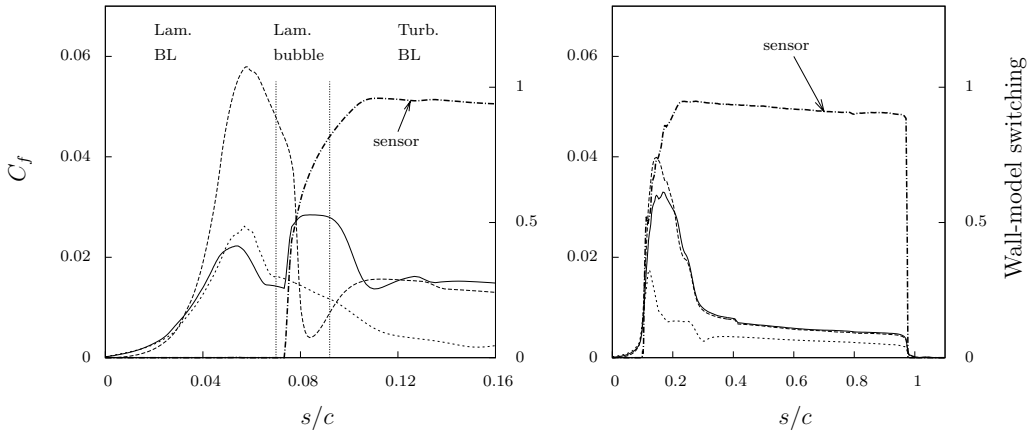

FIGURE 9. *left* - Friction coefficient along the slat. *right* - Friction coefficient along the main element (*right*), starting from the stagnation point. Same legend as in Fig. 8. The sensor curve indicate the time-averaged value of the wall-model switching, a unity value on the right y-axis means that the wall-model was applied at every time step.

Although this sensor is far from perfect, the results show a very good trend and are likely to be further improved with a more elaborate sensor. These results are referred to as the Dynamic Laminar-Turbulent Switching (DLTS) case. The difference obtained in the pressure distibution is hardly noticeable between the DLTS and the WM cases, although the DLTS brings a slight improvement in the integrated aerodynamic coefficients in the slat region. This is in agreement with the calibration of the flow sensor, the threshold of which was chosen based on observations of the flow over the slat. The main element shows the biggest discrepancies, which has to be related to the velocity field prediction in this region; this is discussed below.

4.4. *Results: skin friction and velocity profiles*

We focus here on the prediction of the velocity field, and the differences obtained using the DLTS in comparison with the WM case. Figure 9 gives a better insight into the impact of the DLTS. The level of shear stress in the laminar region of the slat is significantly decreased with the DLTS in contrast with the WM case. The resulting shear stress is close to the NOWM case, as expected in the laminar region. However, this attenuation does not extended to the end of the transition bubble as it should, mainly because the EL is located above the recirculation region. As a consequence, the skin friction coefficient C_f peaks in a region where it should be negative. As mentioned above, the calibration of the sensor was done for the slat flow, which results in relatively poor results for the main element. Indeed, the sensor seems to have a limited effect on the main element, and the computed shear stress is comparable with and without DLTS.

The over-estimation of the shear stress acts as a momentum sink. This is directly observed in the velocity profiles presented in Fig. 10, at different location along the airfoil. The effect of the DLTS can be seen at location P_1, with a considerable reduction in the thickness of the slat-induced shear layer. At this location, the noticeable shift between computation and experiments in the free-stream velocity is consistent with the results of Rumsey *et al.* (1998), who performed full RANS simulations of the same test case. The authors suggested that the error may come from an "improper calibration in the experimental data". The DLTS gives very good results in the flap region, where the

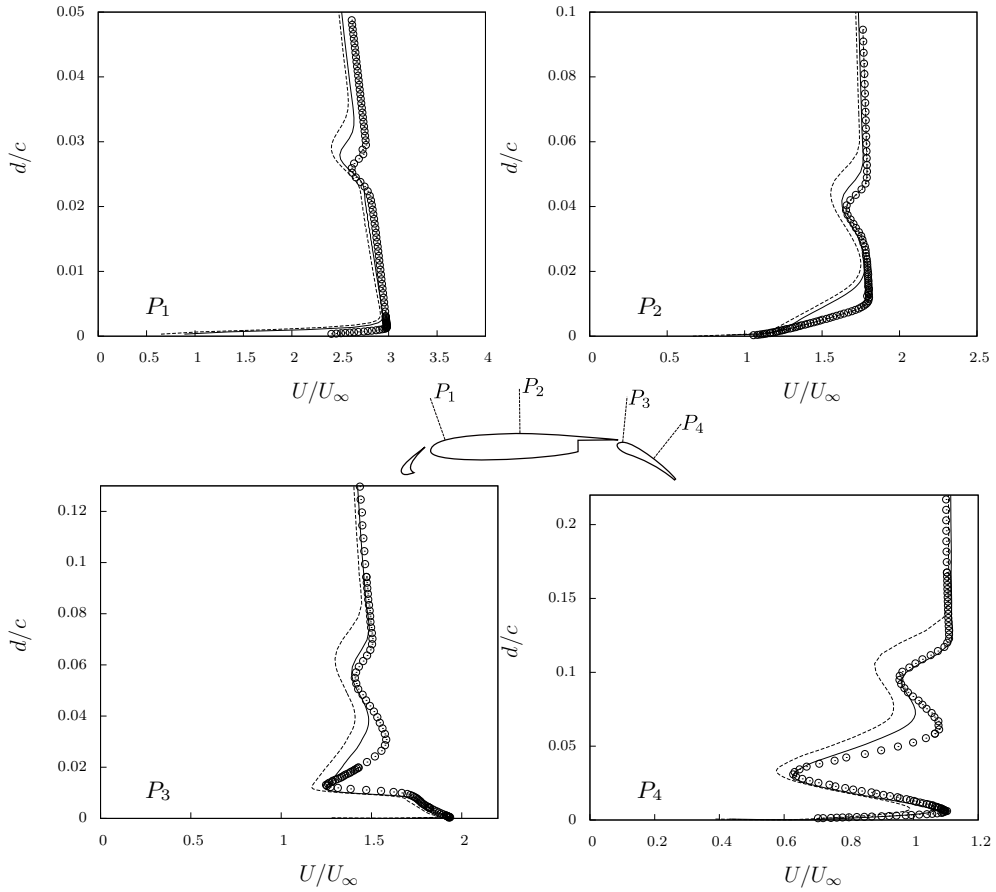

FIGURE 10. Velocity profiles at different locations along the airfoil. (∘) Experiments by Chin *et al.* (1993), (----) WM, (—) DLTS.

boundary layer is fairly well predicted (P_3 and P_4 planes). The large error observed in the boundary layer on the main element is consistent with the inaccurate detection of the transition region by the flow sensor, and can be seen in each profile. We conclude that the prediction of the velocity profiles is very promising, even if they suffer from an over-estimation of the shear stress in some laminar regions. Therefore, handling in a correct way the transition appears to be the most important issue in order to accurately predict the flow field. This issue will be the subject of future work.

5. Conclusions and future work

A wall-model implementation is proposed for general compressible/incompressible solvers on unstructured grids, and tested with the in-house compressible solver CharLES. The additional cost of the wall model is about 30%, but could be reduced to 5% with some optimization of the load-balance. Nevertheless, the computational cost is reduced by two orders of magnitude compared to that of classic wall-resolved LES by (a) reducing the number of grid points by one order of magnitude and (b) increasing the time step by one

order of magnitude because the grid for the wall-modeled LES is much less constrained by the acoustic time-step limitation.

The method is tested on the flow around the McDonnell-Douglas 30P/30N airfoil at a realistic (high) Reynolds number. Preliminary results show a very good agreement for the aerodynamic coefficients, although the velocity field is affected by an over-estimation of the wall shear stress in laminar regions. We demonstrate that a simple sensor, which switches on/off the wall model in turbulent/laminar regions, greatly improves the results. The design of an appropriate flow sensor is thus a key issue in achieving a fully predictive tool for LES of high-Reynolds-numbers, wall-bounded flows. Significant improvements are also expected to come from refinements of the grid, especially at the leading edge of the main element and on the slat. Finally, various angles of attack will be computed to verify that the lift curve is predicted accurately, as well as the point of stall.

Acknowledgments

The work was supported by NASA under the Subsonic Fixed-Wing Program (Grant NNX11AI60A) and by the Boeing Company. Computations were carried out on the Certainty cluster which was funded by NSF. The authors are thankful to Prof. Peter Bradshaw for his valuable comments. This work is dedicated to the memory of Prof. Jean-Bernard Cazalbou, former PhD supervisor of the first author. His wonderful guidance, knowledge and kindness will be greatly missed.

REFERENCES

Balaras, E., Benocci, C. & Piomelli, U. 1996 Two-layer approximate boundary conditions for large eddy simulations. *AIAA J.* **34**, 1111–1119.

Bertelrud, A. 1998 Transition on a three-element high lift configuration at high Reynolds number. *AIAA paper 98-0703* .

Chin, V. D., Peters, D. W., Spaid, F. W. & MacGhee, R. J. 1993 Flowfield measurements about a multi-element airfoil at high Reynolds numbers. *AIAA paper 93-3137* .

Duprat, C., Balarac, G., Métais, O., Congedo, P. M. & Brugière, O. 2011 A wall-layer model for large-eddy simulations of turbulent flows with/out pressure gradient. *Phys. Fluids* **23** (1).

Germano, M., Piomelli, U., Moin, P. & Cabot, W. H. 1991 A dynamic subgrid-scale eddy viscosity model. *Phys. Fluids* **3** (7), 1760–1765.

Hoyas, S. & Jiménez, J. 2006 Scaling of the velocity fluctuations in turbulent channels up to $\mathrm{Re}_\tau = 2000$. *Phys. Fluids* **18** (1).

Kawai, S. & Larsson, J. 2012 Wall-modeling in large eddy simulation: length scales, grid resolution and accuracy. *Phys. Fluids. (In press)* .

Klausmeyer, S. M. & Lin, J. C. 1994 An experimental investigation of skin friction on a multi-element airfoil. *AIAA paper 94-1870* .

Rumsey, C. 2002 Prediction of high lift: review of present CFD capability. *Progress Aerospace Sci.* **38** (2), 145–180.

Rumsey, C. L., Gatski, T. B., Ying, S. X. & Bertelrud, A. 1998 Prediction of high-lift flows using turbulent closure models. *AIAA J.* **36**, 765–774.

Wang, M. & Moin, P. 2002 Dynamic wall modeling for large-eddy simulation of complex turbulent flows. *Phys. Fluids* **14** (7), 2043–2051.